PHYSICAL REVIEW A **87**, 052505 (2013)

High-resolution photoassociation spectroscopy of the ^{6}Li$_2$ $1^3\Sigma_g^+$ state

Mariusz Semczuk,[1] Xuan Li,[2] Will Gunton,[1] Magnus Haw,[1] Nikesh S. Dattani,[3]
Julien Witz,[1] Arthur K. Mills,[1] David J. Jones,[1] and Kirk W. Madison[1]
[1]*Department of Physics and Astronomy, University of British Columbia, Vancouver, Canada*
[2]*Chemical Science Division, Lawrence Berkeley National Laboratory, Berkeley, California 94720, USA*
[3]*Department of Chemistry, University of Oxford, Oxford, United Kingdom*

(Received 21 September 2012; published 9 May 2013)

We present experimental observations of seven vibrational levels, $v' = 20$–26, of the $1^3\Sigma_g^+$ excited state of Li$_2$ molecules by the photoassociation (PA) of a degenerate Fermi gas of ^{6}Li atoms. For each vibrational level, we resolve the rotational structure using a Feshbach resonance to enhance the PA rates from p-wave collisions. We also determine the spin-spin and spin-rotation interaction constants for this state. The absolute uncertainty of our measurements is ± 0.00002 cm^{-1} (± 600 kHz). We use this data to further refine an analytic potential for this state.

DOI: 10.1103/PhysRevA.87.052505 PACS number(s): 33.20.−t, 34.50.−s, 67.85.Lm

I. INTRODUCTION

Photoassociation (PA) of ultracold atoms is a powerful spectroscopic technique that has been used extensively since the advent of laser cooling to make precise measurements of high-lying vibrational levels that are often difficult to access with traditional bound-bound molecular spectroscopy. In addition to improving our knowledge of weakly bound molecular states, PA spectroscopy has also allowed precise determinations of atom-atom scattering lengths and excited atomic state lifetimes. PA resonances have also been used to control atomic interactions via optical Feshbach resonances and for the production of ultracold molecules, as discussed in several excellent review articles [1–5].

In this work, we measure the binding energies of seven vibrational levels, $v' = 20$–26, of the $1^3\Sigma_g^+$ excited state of ^{6}Li$_2$ molecules by photoassociating a quantum degenerate Fermi gas of lithium atoms held in a shallow optical dipole trap. The absolute uncertainty of our measurements is ± 0.00002 cm^{-1} (± 600 kHz). As in previous high-resolution photoassociative spectra of lithium, our frequency resolution allows us to resolve the rotational structure of these levels [6]. In addition, we observe and quantify the spin-spin and spin-rotation coupling constants for this state. As shown in Fig. 1, these measurements bridge a gap between measurements of the deeply lying $v' = 1$–7 levels by Fourier transform infrared (FTIR) spectroscopy (of both ^{7,7}Li$_2$ and ^{6,6}Li$_2$ molecules) [7,8] and measurements of the binding energies of levels $v' = 62$–90 of ^{7,7}Li$_2$ and $v' = 56$–84 of ^{6,6}Li$_2$ by photoassociation of atoms in a magneto-optic trap [9].

The motivations for the present work of mapping the excited-state potential in this wavelength range include the following: (a) these measurements provide an important addition to the existing data allowing us to make a much more complete and accurate, global description of this state; (b) knowing the locations of these intermediate states is important for the eventual formation of ultracold ground triplet state molecules since these states are expected to strike the best compromise between a good Franck-Condon overlap with the initial state (either a Feshbach resonance molecule or an unbound collision state) and the final state in the $a^3\Sigma_u^+$ potential; and (c) this wavelength range is particularly convenient for future experiments since it is easily accessible by both solid-state (Ti:sapphire) and diode lasers. This latter point is relevant to future experiments on the probing, alignment, and spinning of ultracold, weakly bound Li$_2$ molecules (i.e., either Feshbach halo dimers or molecules in the ground triplet state) with high-intensity, ultrashort pulses from Ti:sapphire lasers [11–13]. In such experiments, knowing the excited-state energy levels is important as off-resonant excitation of the ground-state molecule is intended and excited-state transfer should be avoided.

This paper is organized as follows. Section II presents a description of the experimental apparatus and our measurement methodology. In Sec. III, we show several examples of measured spectra, and in Sec. IV, we discuss the interpretation and assignment of the PA spectral features. In Sec. V, we introduce the model for the potential-energy curve for Li$_2$ ($1^3\Sigma_g^+$), and we present refined analytic potentials for this state and the $a^3\Sigma_g^+$ state of ^{6,6}Li$_2$ and ^{7,7}Li$_2$, which were calculated using experimental results from this paper. We conclude with a summary and outlook for future work in Sec. VI.

II. EXPERIMENTAL METHODS

For these measurements, we load a magneto-optic trap (MOT) with 3×10^7 ^{6}Li atoms in 20 s directly from an effusive oven, as described in [14,15]. We then compress and cool the MOT by increasing the axial magnetic field gradient from 40 to 60 G cm^{-1}, lowering the intensity and shifting the frequency of both the "pump" light (near the $2s_{1/2}, F = 3/2 \rightarrow 2p_{3/2}, F = 5/2$ transition frequency) and the "repump" light (near the $2s_{1/2}, F = 1/2 \rightarrow 2p_{3/2}, F = 3/2$ transition frequency) to 10 MHz below resonance. During this compression and cooling phase, a crossed dipole trap (CDT) of 200 W total power is turned on and, in less than 10 ms, 5% of the ^{6}Li atoms are transferred into the CDT. We observe extremely rapid trap losses due to light-assisted collisions and hyperfine relaxation, and we therefore optically pump to the lower hyperfine state ($F = 1/2$) during the transfer by extinguishing the repump light. This procedure produces an almost equal population of the two sublevels of the lower hyperfine state: $|1\rangle \equiv |F = 1/2, m_F = 1/2\rangle$

©2013 American Physical Society

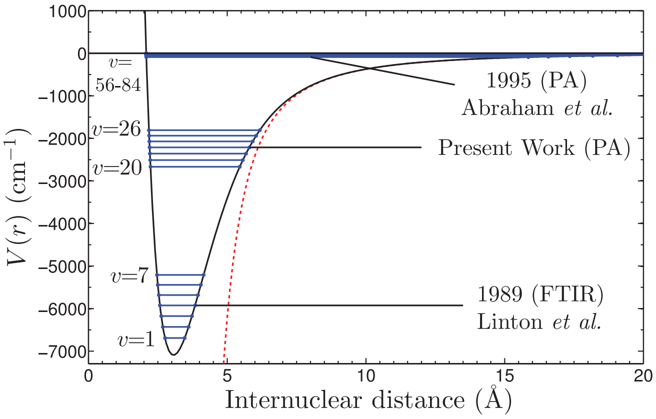

FIG. 1. (Color online) The $1^3\Sigma_g^+$ potential studied in this work (solid line). The solid filled areas indicate regions where experimental data is available for ^{6,6}Li$_2$. The present work includes high-resolution data from seven new vibrational states ($v' = 20$ to 26), including the $N' = 0,1,2$ rotational states in each case. The theoretical long-range potential according to [10] is shown by the dotted line.

and $|2\rangle \equiv |F = 1/2, m_F = -1/2\rangle$. The light for the CDT is derived from a 100 W fiber laser (SPI Lasers, SP-100C-0013) operating at 1090 nm with a spectral width exceeding 1 nm. The CDT is comprised of two nearly copropagating beams crossing at an angle of 14°. Each beam has a maximum power of 100 W (for a total power of 200 W) and is focused to a waist ($1/e^2$ intensity radius) of 42 μm and 49 μm. After the MOT light is extinguished, the CDT beam power is ramped down linearly in time to 100 W total (50 W per beam) in 100 ms, while applying a homogenous magnetic field of 800 G. Rapid thermalization occurs because of the large collision rate induced by a very wide s-wave Feshbach resonance between the $|1\rangle$ and $|2\rangle$ states at 834 G [16]. At the end of this forced evaporation stage, there are approximately 10^6 atoms remaining at a temperature of 200 μK (verified by a time-of-flight expansion measurement). At this point, atoms are transferred into a lower-power CDT which is superimposed on the high-power CDT. The light for this second CDT is generated by a narrow-linewidth (<10 kHz), 20 W fiber laser operating at 1064 nm (IPG Photonics, YLR-20-1064-LP-SF). This transfer is done to avoid ensemble heating observed in the SPI laser CDT and allows further forced evaporative cooling to much lower temperatures. The IPG CDT is comprised of two beams crossing at an angle of 60° and with a total power of 15 W. The beams are focused to a waist ($1/e^2$ intensity radius) of 25 and 36 μm. The IPG CDT beam powers are controlled by two independent acousto-optic modulators and are configured to have a frequency difference of 190 MHz so that the rapidly moving interference pattern generated at the intersection of the two beams has no effect on the atomic motion and the atoms experience the averaged potential of the two beams. After the transfer of atoms into the IPG CDT, the magnetic field is lowered to 300 G, where the s-wave collision cross section between the $|1\rangle$ and $|2\rangle$ states is large enough to continue efficient evaporation. This magnetic field is also chosen because at this value there are no bound molecular states near to the atom-atom threshold into which the atoms can decay via three-body recombination. The goal of this is to produce very cold atomic distributions without also forming Feshbach molecules which would occur for evaporation near the 834 G Feshbach resonance. The trap depth is lowered using a combination of linear and exponential ramps from $U_{\rm trap} = 500$ μK to $U_{\rm trap} = 8$ μK in typically 5 s. At the end of this evaporation step, the ensemble is composed of 3×10^4 atoms with equal populations of the $|1\rangle$ and $|2\rangle$ states, and the temperature (verified by time-of-flight expansion) is 800 nK.

After this preparation step, the magnetic field is lowered to a very small value and PA light from a single-frequency, tunable Ti:sapphire laser beam illuminates the atomic cloud for an exposure (hold) time in the range 0.5–2 seconds. The PA light is a single beam that propagates colinearly with one of the arms of the lower-power CDT and is focused to a waist ($1/e^2$ intensity radius) of 50 μm. The light is linearly polarized and aligned along the direction of the bias magnetic field used for the measurements of p-wave Feshbach enhanced PA. When the bias field is off, there persists a residual magnetic field below 400 mG. For these experiments, the power of the PA light is up to 100 mW, corresponding to an intensity of 1270 W cm^{-2}. When the photon energy $h\nu_{\rm PA}$ equals the energy difference between the unbound state of a colliding atomic pair and a bound molecular excited state, molecules form at a rate proportional to the atom-atom collision rate and atoms are subsequently lost from the trap. This loss occurs because the excited-state molecule either radiatively decays into the unbound continuum of two free atoms with sufficient energy to be lost from the shallow CDT or it decays into a bound-state molecule which is not detected in our atom number measurement. The probability of this latter event can be quite high when exciting particular vibrational levels in the $1^3\Sigma_g^+$ excited state [17]. After this exposure time, the number of atoms remaining is determined by an absorption image of the cloud immediately after the extinction of the CDT.

For some of the measurements presented here, $\nu_{\rm PA}$ was determined by a commercial wave meter (Bristol 621A-NIR) with an absolute accuracy of 60 MHz and a shot-to-shot repeatability (i.e., precision) of 10 MHz in the frequency range of this work. For the high-resolution measurements, the Ti:sapphire laser, operating in the range from 770 to 820 nm, is stabilized to a fiber-based, self-referenced, femtosecond frequency-comb operating with a center wavelength of 1550 nm, as described previously [19]. Briefly, the frequency comb is an erbium-doped, fiber laser frequency comb with two amplified output branches. One branch is used for self-referencing the carrier-envelope offset frequency via an f–$2f$ interferometer. The second branch is also spectrally broadened in a highly nonlinear fiber, but not to a full octave of optical frequencies. The output of this branch is frequency doubled using an array of periodically poled lithium niobate waveguides with different poling periods. The frequency-doubled comb is then mixed with the Ti:sapphire laser on a fast photodiode to generate a heterodyne beatnote, which is used to stabilize the Ti:sapphire laser to the frequency comb. For this work, we verified the comb-referenced Ti:sapphire's absolute frequency uncertainty by measuring the resonant frequencies of the D2 line at 780 nm (the $5s_{1/2}, \rightarrow 5p_{3/2}$ transition) of ^{85}Rb atoms in a vapor cell and comparing them with their known values [18]. We verified that the absolute uncertainty is ±600 kHz, which is consistent with that determined previously [19].

III. OBSERVATIONS

In our initial search of PA resonances, we held the magnetic field near to the s-wave Feshbach resonance between the $|1\rangle$ and $|2\rangle$ states at 834 G to enhance the collision rate. This produced a very wide (1 GHz FWHM) PA loss feature, which facilitated initial detection [20]. After the approximate locations of the PA resonances were found in this way, we performed a high-resolution scan with an ensemble temperature of 15 μK and with no bias magnetic field [21]. We observed that the PA spectrum of each vibrational level had associated with it three narrow (below 10 MHz FWHM) features distributed across a range of 0.7 GHz, as shown in Fig. 2. Figure 3 shows a higher-resolution scan of the second feature shown in Fig. 2. In order to reduce as much as possible the thermal broadening and the inhomogeneous ac Stark shift produced by the optical dipole trapping potential, these data were obtained in a very shallow trap ($U_{\mathrm{trap}}/k_{\mathrm{B}} \sim 8\ \mu$K) and at an ensemble temperature of 800 nK, which is a temperature well below the Fermi temperature for this two-component Fermi gas ($T/T_{\mathrm{F}} = 0.4$). We then verified that these PA resonances arise from collisions between atoms in states $|1\rangle$ and $|2\rangle$ by using a state-selective resonant pulse of light to remove all atoms in either of the two states. The spin purification was done at the end of the preparation sequence, and we observed the absence of these atom loss features with either one of the states removed [22]. To rule out the absence of these loss features due to a simple reduction of the density, we observed a reappearance of the PA features when using an incoherent mixture of the $|1\rangle$ and $|2\rangle$ states with the same total number of particles and temperature as the ensembles after spin purification. Given that p-wave collisions are dramatically suppressed at these temperatures and that these PA loss features were visibly enhanced by the s-wave Feshbach resonance (FR), we inferred that they arise from s-wave collisions between atoms in states $|1\rangle$ and $|2\rangle$. Thus, they correspond to a transition from an initial unbound molecular state with $N = 0$, $G = 0$ to an excited state with $N' = 1$, $G' = 0$ (assuming G is a good quantum number). As we describe later, we find that spin-spin and spin-rotation coupling split the excited state into three sublevels, producing the three PA features. In this case, G is no longer a good quantum number. The locations of these three features for each of the seven vibrational levels is provided in Table I.

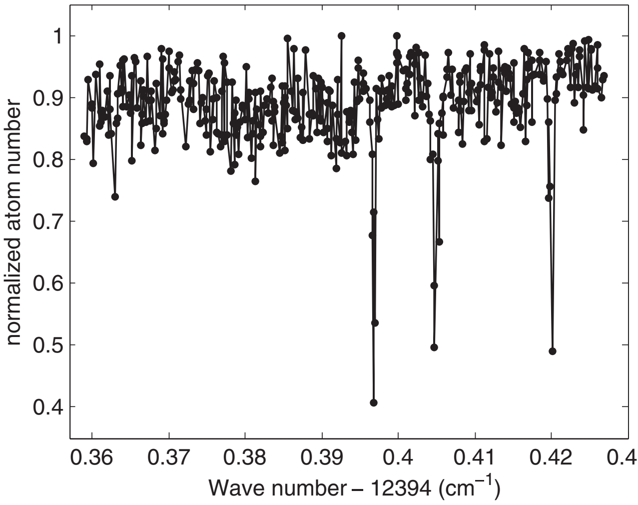

FIG. 2. Normalized ^{6}Li atom number as a function of photoassociation laser energy $h\nu_{\mathrm{PA}}$ after a 2 s hold time with zero-bias magnetic field and a PA laser intensity of $I_{\mathrm{PA}} = 635$ W cm^{-2}. These three resonances correspond to a transition from an initial unbound molecular state with $N = 0$, $G = 0$ to the $v' = 21$ vibrational level of the $1^3\Sigma_g^+$ excited state with $N' = 1$, $G' = 0$. The ensemble temperature was 15 μK.

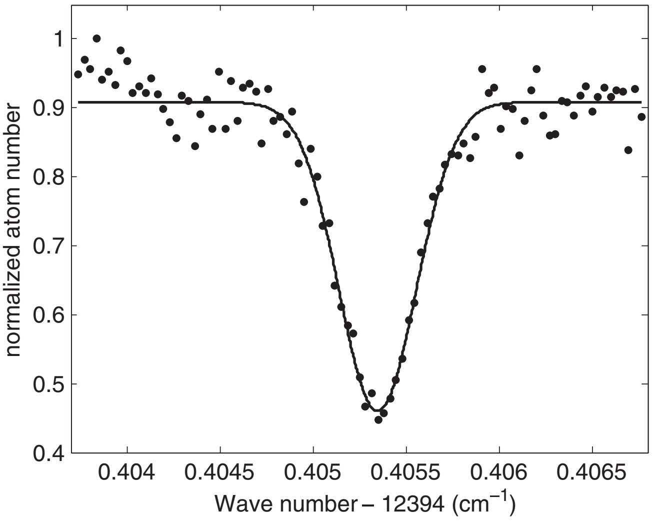

FIG. 3. High-resolution scan of the normalized ^{6}Li atom number as a function of photoassociation laser energy $h\nu_{\mathrm{PA}}$ after a 750 ms hold time with zero-bias magnetic field and a PA laser intensity of $I_{\mathrm{PA}} = 635$ W cm^{-2}. This is the second of the three resonances shown in Fig. 2 corresponding to a transition from an initial unbound molecular state with $N = 0$, $G = 0$ to the $v' = 21$ vibrational level of the $1^3\Sigma_g^+$ excited state with $N' = 1$, $G' = 0$. The ensemble temperature was 800 nK. The FWHM of this loss peak is 0.00048 cm^{-1} (14.4 MHz).

TABLE I. Experimentally measured PA resonances for s-wave collisions in an incoherent mixture of the $|1\rangle$ and $|2\rangle$ states of ^{6}Li. These three PA resonances correspond to a transition from an initial unbound molecular state with $N = 0$, $G = 0$ to the vth vibrational level of the $1^3\Sigma_g^+$ excited state with $N' = 1$. As we explain in Sec. IV, spin-spin and spin-rotation coupling split the excited state into three sublevels, producing the three PA features corresponding to quantum numbers ($N' = 1$, $J' = 1$), ($N' = 1$, $J' = 2$), and ($N' = 1$, $J' = 0$), respectively. The absolute uncertainty in each of these measurements is ±0.00002 cm^{-1} (±600 kHz).

v'	First (cm^{-1})	Second (cm^{-1})	Third (cm^{-1})
20	12237.17755	12237.18587	12237.20126
21	12394.39726	12394.40535	12394.42039
22	12546.06767	12546.07552	12546.09025
23	12692.17316	12692.18080	12692.19509
24	12832.70080	12832.70820	12832.72214
25	12697.64147	12967.64862	12967.66219
26	13096.99114	13096.99804	13097.01125

We also located for each of the vibrational states the PA resonances associated with p-wave ground-state collisions. However, these features were *only* observable in our experiment when measures were taken to enhance the PA scattering rate. In order to observe these PA resonances, we enhanced the p-wave scattering rate by stopping the evaporation at an ensemble temperature of 250 μK and by holding the magnetic field at 185 G during the PA stage. This magnetic field is near the p-wave Feshbach resonance between the $|1\rangle$ and $|2\rangle$ states at 185.1 G [16]. Due to the Feshbach-resonance enhancement of inelastic ground-state collisions, the ensemble particle loss in the absence of the PA light was approximately 50% during the 2 s hold time. Additional loss was induced when the light was near a PA resonance. Figure 4 shows the loss spectrum for a transition from an initial unbound molecular state with $N = 1$, $G = 1$ to the $v' = 20$ vibrational level of the $1^3\Sigma_g^+$ excited state with $N' = 2$, $G' = 1$. For each of the seven vibrational levels, we observed at least four (three) distinct loss features for transitions to the $N' = 2$, $G' = 1$ ($N' = 0$, $G' = 1$) final state. By evaporating the ensemble to 15 μK and holding the magnetic field at 184.7 G, we observed that each of these loss features results from multiple PA resonances that are unresolvable at 250 μK. The locations of the loss features observed at 250 μK for each of the seven vibrational levels is provided in Tables II and III. These measurements were performed in the absence of the comb stabilization. Instead, the Ti:sapphire laser was locked to an external cavity and its frequency was measured with the wave meter whose uncertainty is 60 MHz.

TABLE II. Experimentally measured PA resonances for p-wave collisions in an incoherent mixture of the $|1\rangle$ and $|2\rangle$ states of ^{6}Li held at a magnetic field of $B = 185$ G. Each of these values was extracted by fitting a loss spectrum like that shown in Fig. 4. These PA resonances correspond to a transition from an initial unbound molecular state with $N = 1$, $G = 1$ to the vth vibrational level of the $1^3\Sigma_g^+$ excited state with $N' = 0$, $G' = 1$. While the precision in these measurements is 0.001 cm^{-1}, the uncertainty, limited by the wave meter, is ±0.002 cm^{-1}.

v'	First (cm^{-1})	Second (cm^{-1})	Third (cm^{-1})
20	12236.388	12236.407	12236.424
21	12393.629	12393.648	12393.664
22	12545.320	12545.338	12545.355
23	12691.446	12691.465	12691.480
24	12831.995	12832.012	12832.029
25	12966.957	12966.975	12966.991
26	13096.326	13096.346	13096.362

Characterization of systematic shifts

While the absolute uncertainty of our PA measurements made using the frequency comb is ±600 kHz, the data was taken in the presence of a small but nonzero magnetic field and in an optical dipole trap with a known intensity. These residual fields as well as the PA laser itself can lead to a systematic shift of the resonance positions from their zero-field values. Therefore, in an effort to quantify the role of the PA laser intensity, the CDT laser intensity, and the residual magnetic field on the PA loss features, we varied each one and measured the PA resonance position and width for various excited states. In each case, we assumed a linear dependence and determined a shift rate of the resonance position with the corresponding field strength. The uncertainty in this rate is a one-σ statistical uncertainty on the slope of the linear fit.

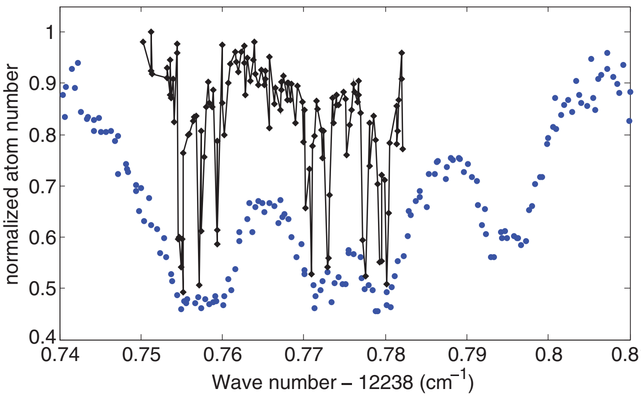

FIG. 4. (Color online) Normalized ^{6}Li atom number as a function of photoassociation laser energy $h\nu_{\mathrm{PA}}$ after a 2 s hold time. The circles are for an ensemble temperature of 250 μK at 185 G, and four distinct features are observed. The diamonds denote the atom loss for an ensemble temperature of 15 μK and at a magnetic field of 184.7 G. At this lower temperature, these loss features are seen to result from multiple PA resonances that are unresolvable at 250 μK. These PA features arise from p-wave ground-state collisions and are enhanced by proximity to a p-wave Feshbach resonance between the $|1\rangle$ and $|2\rangle$ states at 185.1 G.

When varying the PA laser intensity from $I_{\mathrm{PA}} = 0.19$ kW cm^{-2} to $I_{\mathrm{PA}} = 1.27$ kW cm^{-2}, we observed that the centroid of the first feature ($J' = 1$) associated with the $v' = 26$ excited state shifted to higher frequencies at a rate of 471 ± 433 kHz per kW cm^{-2}. When the CDT laser intensity was varied from 5.4 kW cm^{-2} (145 mW total CDT power) to 140 kW cm^{-2} (3.1 W total CDT power), the PA feature centroid associated with the $v' = 24$, $J' = 1$ state shifted down in frequency at a rate of $-(19 \pm 1.2)$ kHz per kW cm^{-2}. The

TABLE III. Experimentally measured PA resonances for p-wave collisions in an incoherent mixture of the $|1\rangle$ and $|2\rangle$ states of ^{6}Li held at a magnetic field of $B = 185$ G. Each of these values was extracted by fitting a loss spectrum like that shown in Fig. 4. These PA resonances correspond to a transition from an initial unbound molecular state with $N = 1$, $G = 1$ to the vth vibrational level of the $1^3\Sigma_g^+$ excited state with $N' = 2$, $G' = 1$. While the precision in these measurements is 0.001 cm^{-1}, the uncertainty, limited by the wave meter, is ±0.002 cm^{-1}.

v'	First (cm^{-1})	Second (cm^{-1})	Third (cm^{-1})	Fourth (cm^{-1})
20	12238.757	12238.772	12238.780	12238.795
21	12395.936	12395.951	12395.958	12395.973
22	12547.567	12547.579	12547.587	12547.601
23	12693.628	12693.642	12693.648	12693.665
24	12834.113	12834.128	12834.134	12834.150
25	12969.011	12969.026	12969.032	12969.047
26	13098.315	13098.332	13098.339	13098.355

resonance positions reported in Table I were determined using a PA laser intensity of $I_{\mathrm{PA}} = 635$ W cm^{-2} and a CDT intensity of 7.5 kW cm^{-2}. Assuming the differential ac Stark shift is the same for all excited states, the reported values are therefore shifted lower by 142 ± 9 kHz due to the CDT and higher by 300 ± 274 kHz due to the PA laser than their extrapolated position at zero-differential ac Stark shift. The overall ac Stark shift of the resonance positions is thus higher by 157 kHz with an uncertainty of ±274 kHz. Both this shift and uncertainty are small compared to the absolute uncertainty of the frequency comb. For the resonance positions reported in Tables II and III, the trapping power was larger (40 W total) and the differential ac Stark shift due to the CDT is estimated to be $-(15 \pm 1)$ MHz.

When the magnetic field was varied from 0 to 10 G, the PA features associated with the $v' = 24$, $J' = 1$, $J' = 2$, and $J' = 0$ states were observed to shift and, in the case of $J' = 1$ and $J' = 2$, to broaden and eventually split into multiple resolvable peaks. In each case, we measured the PA feature center of mass and found that when the magnetic field was varied from 0 to 1 G, the barycenter of the PA features moved by $-(91.2 \pm 18.3)$ kHz for the $J' = 1$ state, $+(46 \pm 28)$ kHz for the $J' = 2$ state, and $+(74.5 \pm 30.1)$ kHz for the $J' = 0$ state. Since the resonance positions reported in Table I were determined in the presence of a residual magnetic field below 400 mG, the uncertainty in their positions due to the magnetic field was below 50 kHz for all J states and thus small compared to the absolute uncertainty of the frequency comb.

IV. INTERPRETATION

In order to interpret our measurements, we begin with a brief review of the symmetry properties and corresponding selection rules relevant for the photoassociation process. Molecules in the $1^3\Sigma_g^+$ excited state are characterized by the Hund's case "b" coupling scheme in which the total electronic (nuclear) spin $\vec{S} = \vec{s}_1 + \vec{s}_2$ ($\vec{I} = \vec{i}_1 + \vec{i}_2$) is completely uncoupled from the internuclear axis. Here, $\vec{s}_j$ ($\vec{i}_j$) is the electronic (nuclear) spin of atom "j". This occurs when $\Lambda = 0$, i.e., the projection of the orbital angular momentum of the electrons along the internuclear axis is zero, and there is therefore no axial magnetic field to couple the total spin to the axis. For "Σ" states, the orbital angular momentum of the electrons is zero and therefore Λ is always identically zero; however, even in some cases where $\Lambda \neq 0$, especially for light molecules, the coupling is sufficiently weak that Hund's case b is still the appropriate scheme [23]. The total angular momentum, apart from the spin, is $\vec{K} \equiv \vec{N} + \vec{\Lambda}$, i.e., the vector sum of $\vec{\Lambda}$ and the rotational angular momentum of the nuclei $\vec{N}$. Therefore, for Σ states, $\vec{K} = \vec{N}$, and thus $\vec{K}$ is perpendicular to the internuclear axis. The total spin of the molecule is $\vec{G} = \vec{S} + \vec{I}$ and is a good quantum number so long as the hyperfine interaction and spin-rotational couplings are small. The total spin ($\vec{G}$) combines with the total angular momentum apart from spin ($\vec{K}$) to result in the total angular momentum including spin as $\vec{J} = \vec{K} + \vec{G}$.

For electric dipole radiation, the selection rule is that $\Delta J = 0, \pm 1$ with the restriction that $J = 0 \not\leftrightarrow J = 0$. In addition, under the emission or absorption of a photon, the parity of the electronic orbital must change ($+ \leftrightarrow -$), and for a homonuclear molecule, the symmetry of the coordinate function under the interchange of the two nuclei must change from symmetric to antisymmetric, or vice versa ($g \leftrightarrow u$). In the present scenario of Hund's case b coupling, the spin is so weakly coupled to the other angular momenta that both quantum numbers S and K are well defined and we have, in addition, the selection rules $\Delta S = 0$ (or, equivalently, $\Delta G = 0$) and therefore $\Delta K = 0, \pm 1$ with the restriction that $\Delta K = 0$ is forbidden for $\Sigma \rightarrow \Sigma$ transitions. Since we are here only concerned with transitions to the $1^3\Sigma_g^+$ excited state, we have that $\Delta N = \pm 1$ and $\Delta G = 0$.

We now discuss the allowed quantum numbers for the initial and final states. In this work, we only consider collisions between two ^{6}Li atoms, which are composite fermions (consisting of 9 fermions: 3 protons, 3 neutrons, and 3 electrons), and we note that the two-body eigenstates, composed of a spin part and an orbital part, must be antisymmetric upon exchange of the two atoms. The consequence is that only certain spin states are possible given a particular orbital state. An important example of this constraint imposed by exchange symmetry is that the two-body position wave function (sometimes called the "coordinate function" or orbital state) must be antisymmetric for a collision between two fermions in the same spin state (for which the spin wave function is manifestly symmetric). Thus, a spin-polarized Fermi gas can only have odd partial wave collisions (p-, f-, h-wave, etc.) corresponding to odd values of the rotational angular momentum of the complex ($N = 1,3,5,\ldots$), which are antisymmetric with respect to atom exchange. For a gas composed of two distinct spin states, even partial wave collisions can occur (s-, d-, g-wave, etc.) so long as the spin wave function is antisymmetric upon atom exchange. As we described in Sec. III, the ability to turn off s-wave collisions by spin polarizing the gas is a useful feature of our system that we use to validate our assignment of the PA lines.

The total spin angular momentum of the initial unbound molecular state is given by the vector sum of the f quantum numbers for the isolated atoms: $\vec{G} = \vec{f}_1 + \vec{f}_2$. Here, $\vec{f}_1 = \vec{s}_1 + \vec{i}_1$. In our experiment, the atoms are optically pumped to the lowest hyperfine state before being exposed to the photoassociation light. Therefore, we have that $f_1 = f_2 = \frac{1}{2}$ and there are two allowed values of the total spin: $G = 0,1$. Certain values of G (specifically, $G = f_1 + f_2, f_1 + f_2 - 2, \ldots$) are associated with spin states symmetric with respect to the interchange of the atoms, while the orbital states with even values of N are symmetric under the interchange of the atoms. Therefore, all even partial wave collisions ($N = 0,2,4,\ldots$) have a total spin of zero ($G = 0$) and all odd partial wave collisions ($N = 1,3,5,\ldots$) have a total spin of one ($G = 1$).

The final state is a molecule in the $1^3\Sigma_g^+$ potential. For this triplet state, the total electronic spin is well defined ($S = 1$) and the "gerade" symmetry signified by a subscript "g" denotes that all states with an even rotational quantum number ($N = 0,2,4,\ldots$) are symmetric under the interchange of the two nuclei. Because the electronic spin is well defined and fixed for this excited state, we now consider interchanging just the *nuclei* while leaving the electrons untouched. There are three possible values of the total nuclear spin ($I = 0,1,2$) since the nuclear spin of each atom is $i = 1$. Similar to the symmetry of G, states with $I = i_1 + i_2, i_1 + i_2 - 2, \ldots$

TABLE IV. Allowed rotational levels and corresponding nuclear spin configurations for ^{6}Li$_2$ molecules in the limit that spin-spin and spin-rotation couplings are small enough that G is a good quantum number.

State	Electronic spin	Nuclear spin	Allowed rotational states	Total spin
		Ground states		
			$N = 0,2,4,\ldots$	$G = 0$
			$N = 1,3,5,\ldots$	$G = 1$
		Excited states		
$1^3\Sigma_g^+$:	$S = 1$	$I = 0$	$N = 0,2,4,\ldots$	$G = 1$
		$I = 1$	$N = 1,3,5,\ldots$	$G = 0,1,2$
		$I = 2$	$N = 0,2,4,\ldots$	$G = 1,2,3$

(corresponding here to $I = 0$ and $I = 2$) are symmetric with respect to the interchange of the nuclei, whereas the $I = 1$ state is antisymmetric. Since the nuclei are *bosons*, the total wave function must be symmetric under the interchange of the nuclei. Putting this together, we have that the even (odd) values of I occur with even (odd) values of N. The total spin angular momentum quantum number G can take on all values between and including $|I + S|$ and $|I - S|$.

The possible quantum numbers for the ground and excited states are tabulated in Table IV. For a ground-state s-wave collision ($N = 0$), we find that there is only one allowed value for the total spin: $G = 0$. From an initial state with $N = 0$ and $G = 0$, we see that there is only one possible transition to the excited triplet state: $(N = 0,\ G = 0) \rightarrow (N' = 1,\ G' = 0)$. For a ground-state p-wave collision, the initial state is $(N = 1,\ G = 1)$ and there are two possible transitions to the excited triplet state: $(N = 1,\ G = 1) \rightarrow (N' = 0,\ G' = 1)$ and $(N = 1,\ G = 1) \rightarrow (N' = 2,\ G' = 1)$. In both cases, there are two possible values of the total nuclear spin: $I = 0$ or 2.

In the preceding discussion, we have assumed that both the spin-spin coupling and the coupling of the total electronic spin $\vec{S}$ with the molecular rotation $\vec{N}$ are negligible. In this case, the total spin (characterized by $\vec{G}$) is a good quantum number. However, while these couplings are small, we nevertheless do resolve a splitting of the excited-state energy levels by observing three PA resonances, as seen in Fig. 2, instead of a single feature for an initial s-wave collision. As we explain later, the ground state is not split in this particular case because $N = 0$.

In order to properly label the three PA resonances (associated with ground-state s-wave collisions) observed for each rovibrational state given spin-spin and spin-rotational coupling, we redefine $\vec{J}$ to be the total angular momentum *apart from nuclear spin*, $\vec{J} \equiv \vec{N} + \vec{S}$. Here, a magnetic coupling between $\vec{S}$ and $\vec{N}$ (involving an interaction with an effective Hamiltonian of the form $\hat{H}_{\text{spin-rot}} = \gamma_v \vec{N} \cdot \vec{S}$) as well as a spin-spin coupling term (of the form $\hat{H}_{\text{spin-spin}} = 2\lambda_v[\hat{S}_z^2 - \hat{S}^2/3]$) cause a splitting of the rotational levels, previously labeled by N, according to the J quantum number, given by $J = (N + S),\ (N + S - 1),\ (N + S - 2), \ldots, |N - S|$. Therefore, each level with a given $N(\geqslant S)$ consists of $2S + 1$ sublevels, and the number of sublevels is equal to the spin multiplicity. However, for $N < S$, the number of sublevels is equal to $2N + 1$ (the rotational multiplicity). Hence, all $N = 0$ levels do not split, as mentioned previously. For a particular rovibrational state $|v,N\rangle$, with a total spin $S = 1$, the rotational energy is given by [23,24]

$$\begin{aligned} F_{J=N+1} &= B_v N(N+1) + (2N+3)B_v - \lambda_v \\ &\quad - \sqrt{(2N+3)^2 B_v^2 + \lambda_v^2 - 2\lambda_v B_v} + \gamma_v (N+1), \\ F_{J=N} &= B_v N(N+1), \qquad (1) \\ F_{J=N-1} &= B_v N(N+1) - (2N-1)B_v - \lambda_v \\ &\quad + \sqrt{(2N-1)^2 B_v^2 + \lambda_v^2 - 2\lambda_v B_v} - \gamma_v N, \end{aligned}$$

where λ_v and γ_v are constants. Here, λ_v is related to the spin-spin interaction and it describes the coupling between the total spin $\vec{S}$ and the molecular axis; γ_v is related to the spin-rotation interaction and it is a measure of the coupling between $\vec{S}$ and $\vec{N}$. Under most circumstances, these two constants describe small effects which are not spectroscopically resolvable and are typically ignored in the Dunham expansion. However, at the level of resolution in the current experiment, one needs to take into account these second-order perturbations. In the case where spin-spin and spin-rotation couplings are small ($B_v \gg |\lambda_v|, |\gamma_v|$), we can simplify Eq. (1) to

$$\begin{aligned} F_{J=N+1} &= B_v N(N+1) - \frac{2N+2}{2N+3}\lambda_v + \gamma_v(N+1), \\ F_{J=N} &= B_v N(N+1), \qquad (2) \\ F_{J=N-1} &= B_v N(N+1) - \frac{2N}{2N-1}\lambda_v - \gamma_v N. \end{aligned}$$

In addition, when spin-spin coupling is much more important than spin-rotation coupling ($|\lambda_v| \gg |\gamma_v|$), the energy ordering results from the λ_v terms, and we can label these three peaks in Table I, energetically from low to high, as $(N' = 1,\ J' = 1)$, $(N' = 1,\ J' = 2)$, and $(N' = 1,\ J' = 0)$ because λ_v is negative.

Using the peak spacings reported in Table I and Eq. (2), we extract the two parameters, λ_v and γ_v. The determined λ_v constants as a function of v' are plotted in Fig. 5. The dashed line is provided to show its trend. These results agree well with the previous *ab initio* calculation for lithium diatoms [25]. By using Fig. 3 of Ref. [25] and averaging $\lambda(R)$ over the internuclear distance R using the wave functions corresponding to the eigenfunctions of the excited-state potential curve we refined with our data, $\lambda_v \equiv \langle \Phi_v(R)|\lambda(R)|\Phi_v(R)\rangle$,we estimate these *ab initio* λ_v constants for all v' states and plot those also in Fig. 5. Note that the uncertainty of the *ab initio* results given in Fig. 5 is estimated to be a few tens of MHz. This results from the estimated error of the original *ab initio* calculation (a few percent corresponding to ≈10–30 MHz) and the error (≈10 MHz) associated with our digitization of the data in Fig. 3 from Ref. [25], as well as the fact that the *ab initio* calculation was likely done for ^{7,7}Li$_2$ rather than ^{6,6}Li$_2$.

This comparison of λ_v obtained from experimental data and that obtained from *ab initio* calculations clearly demonstrates the validity of the current model to label separate peaks in Table I. The values for λ_v and γ_v determined from our data are provided in Table V. The uncertainty in these parameters is estimated to be ±400 kHz and results from the uncertainty in the PA resonance positions. Using Eq. (1), we verified that

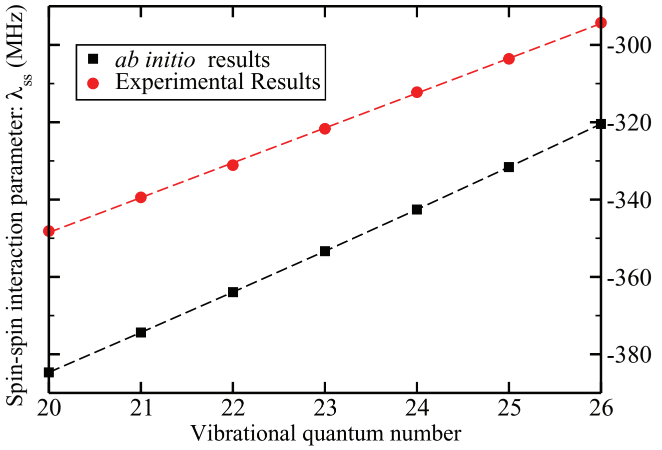

FIG. 5. (Color online) The experimentally determined (circles) and *ab initio* computed (squares) spin-spin interaction constants λ_v as a function of the vibrational quantum number for the $1^3\Sigma_g^+$ electronic state. These constants were determined from the frequency splittings of the three features observed for the $N = 0 \rightarrow N' = 1$ transition. The uncertainty in these values is estimated to be ±400 kHz. The dashed lines are guides to the eye.

the uncertainty in the exact value for B_v is not expected to contribute significantly to the uncertainty in these parameters. We note that this is a direct measurement of the spin-spin and spin-rotation coupling constants in a diatomic lithium system.

The interpretation of the PA resonances arising from p-wave ground-state collisions requires a model to fully account for the hyperfine structure and Zeeman splitting of the ground and excited states at the nonzero magnetic field used. This analysis is a subject for future work.

V. REFINED POTENTIAL

The Morse/long-range (MLR) model for potential-energy functions was first introduced in 2006 [26,27] and major developments were made in 2009 [28] and 2011 [29]. Over these years, the MLR and related models have been very successful in representing the internuclear potentials for dozens of diatomic and polyatomic molecules [26–40].

A particular advantage of the MLR model is that it is a single analytic function that very naturally represents the correct shape of the potential function in good agreement with the experimentally observed energies, while also providing an accurate description of the potential's long-range region according to theory. This makes the MLR model especially convenient to use when the known experimental energies are sparse. For example, the most comprehensive study of $\mathrm{Li}_2(1^3\Sigma_g^+)$ in existence before this work [38] only had a small amount of data available near the bottom of the potential well, and a small amount at the top (see Fig. 1). In that case, since the MLR model is a single analytic function, it was able to interpolate between those two regions very well (see column 4 of Table VIII).

TABLE V. The values for the spin-spin interaction constant λ_v and the spin-rotation interaction constant γ_v determined from Eq. (2) and the peak spacings reported in Table I. The uncertainty in these values is ±400 kHz. The λ_v values are plotted in Fig. 5, along with their expected values determined from *ab initio* calculations.

v'	λ_v (MHz)	γ_v (MHz)
20	− 348.2	− 14.5
21	− 339.4	− 14.5
22	− 331.1	− 14.7
23	− 321.7	− 14.2
24	− 312.2	− 14.4
25	− 303.6	− 14.0
26	− 294.3	− 14.3

In this section, we report a refined version of the $\mathrm{Li}_2(1^3\Sigma_g^+)$ MLR potential from [38] that now incorporates the $J = N = 1$ energies of the seven additional vibrational levels studied in this paper. Various candidate MLR potentials were calculated by direct potential fits (DPFs), where the parameters of the potential are optimized so that the predicted Schrödinger eigenenergies match the experimental energies as closely as possible. We used the same Hamiltonian form as in [38] (see Eq. (3) of [38] and its surroundings), and the least-squares fitting was computed with the publicly available free computer program `DPotFit` [41]. The $\mathrm{MLR}_{p,q}^{r_{\mathrm{ref}}}(N_\beta)$ models for Li_2 that were used as candidates for this refined potential, were defined the same way as those in [38].

These models are defined by

$$V_{\mathrm{MLR}}(r) \equiv \mathfrak{D}_e \left[1 - \frac{u_{\mathrm{LR}}(r)}{u_{\mathrm{LR}}(r_e)} e^{-\beta(r) y_p^{r_e}(r)} \right]^2 , \tag{3}$$

where $\mathfrak{D}_e$ is the dissociation energy, r_e is the equilibrium internuclear distance, and $\beta(r)$ is

$$\beta(r) \equiv \beta_{p,q}^{r_{\mathrm{ref}}}(r) \equiv \beta_\infty y_p^{r_{\mathrm{ref}}}(r) + \left[1 - y_p^{r_{\mathrm{ref}}}(r)\right] \sum_{i=0}^{N_\beta} \beta_i \left[y_q^{r_{\mathrm{ref}}}(r)\right]^i , \tag{4}$$

with

$$\beta_\infty \equiv \lim_{r\to\infty} \beta(r) = \ln \left[\frac{2\mathfrak{D}_e}{u_{\mathrm{LR}}(r_e)} \right] . \tag{5}$$

Equations (3) and (4) also depend on the radial variable

$$y_n^{r_{\mathrm{ref}}}(r) = \frac{r^n - r_{\mathrm{ref}}^n}{r^n + r_{\mathrm{ref}}^n} , \tag{6}$$

where the reference distance r_{ref} may simply be the equilibrium distance r_e as explicitly written in Eq. (3), but adjusting it can significantly reduce the required value of N_β in Eq. (4) for an accurate fit to the experimental data and more consistent predictions of the physical parameters in the model (see, for example, Fig. 5 of [38]). The Šurkus power n is an integer greater than or equal to 1, which is also adjusted to optimize the fit.

Finally, the definition of $u_{\mathrm{LR}}(r)$ depends more on the system being modeled. For large r, Eq. (3) usually has the form $V(r) \simeq \mathfrak{D}_e - u_{\mathrm{LR}}(r)$ [28]; therefore, defining $u_{\mathrm{LR}}(r)$ to be the true theoretical long-range difference between $\mathfrak{D}_e$ and $V(r)$ is often a good starting choice. As described in [10], for very large internuclear distances, the potential energy of $\mathrm{Li}_2(1^3\Sigma_g^+)$ is given by $\mathfrak{D}_e - \lambda_{\mathrm{min}}(r)$, so $\lambda_{\mathrm{min}}(r)$ can be a good first choice for $u_{\mathrm{LR}}(r)$. $\lambda_{\mathrm{min}}(r)$ is defined as the lowest eigenenergy of the (symmetric) matrix that describes the near-dissociation interaction of the $1^3\Sigma_g^+$ state with the nearby $1^1\Pi_g$ and $1^3\Pi_g$ states. When exchange energy terms and the factors describing the relativistic retardation effect are neglected, this matrix is [10]

$$-\begin{pmatrix} \frac{1}{3}\sum\limits_{\substack{m=3,6,8,\\9,10,11,\ldots}}\frac{C_m^{^3\Sigma_g^+}+C_m^{^1\Pi_g}+C_m^{^3\Pi_g}}{r^m} & \frac{1}{3\sqrt{2}}\sum\limits_{\substack{m=3,6,8,\\9,10,11,\ldots}}\frac{-2C_m^{^3\Sigma_g^+}+C_m^{^1\Pi_g}+C_m^{^3\Pi_g}}{r^m} & \frac{1}{\sqrt{6}}\sum\limits_{\substack{m=3,6,8,\\9,10,11,\ldots}}\frac{-C_m^{^1\Pi_g}+C_m^{^3\Pi_g}}{r^m} \\ \frac{1}{3\sqrt{2}}\sum\limits_{\substack{m=3,6,8,\\9,10,11,\ldots}}\frac{-2C_m^{^3\Sigma_g^+}+C_m^{^1\Pi_g}+C_m^{^3\Pi_g}}{r^m} & \Delta E+\frac{1}{6}\sum\limits_{\substack{m=3,6,8,\\9,10,11,\ldots}}\frac{4C_m^{^3\Sigma_g^+}+C_m^{^1\Pi_g}+C_m^{^3\Pi_g}}{r^m} & \frac{1}{2\sqrt{3}}\sum\limits_{\substack{n=3,6,8,\\9,10,11,\ldots}}\frac{-C_m^{^1\Pi_g}+C_m^{^3\Pi_g}}{r^m} \\ \frac{1}{\sqrt{6}}\sum\limits_{\substack{m=3,6,8,\\9,10,11,\ldots}}\frac{-C_m^{^1\Pi_g}+C_m^{^3\Pi_g}}{r^m} & \frac{1}{2\sqrt{3}}\sum\limits_{\substack{m=3,6,8,\\9,10,11,\ldots}}\frac{-C_m^{^1\Pi_g}+C_m^{^3\Pi_g}}{r^m} & \Delta E+\frac{1}{2}\sum\limits_{\substack{m=3,6,8,\\9,10,11,\ldots}}\frac{C_m^{^1\Pi_g}+C_m^{^3\Pi_g}}{r^m} \end{pmatrix}, \tag{7}$$

where ΔE is the (positive) difference between the $^2P_{1/2}$ and $^2P_{3/2}$ atomic spin-orbit levels, $C_3 \equiv C_3^{^{2S+1}\Lambda_g^{(+/-)}}$ are the resonant dipole-dipole interaction terms, and when $m > 3$, $C_m \equiv C_m^{^{2S+1}\Lambda_g^{(+/-)}}$ are the dispersion interaction terms. Note the overall negative sign which reflects that our convention is the opposite to that in [10], where this matrix was first defined in this form.

Using quantum electrodynamics, it has been shown (see [42] and references therein) that the relativistic retardation effect can be described for large r by making the following modifications in Eq. (7):

$$C_3^{^3\Sigma_g^+} \rightarrow C_3^{^3\Sigma_g^+}\left[\cos\left(\frac{r}{\lambda}\right)+\left(\frac{r}{\lambda}\right)\sin\left(\frac{r}{\lambda}\right)\right] \equiv C_{3,\mathrm{ret}}^{^3\Sigma_g^+}(r), \tag{8}$$

$$C_3^{^{2S+1}\Pi_g} \rightarrow C_3^{^{2S+1}\Pi_g}\left[\cos\left(\frac{r}{\lambda}\right)+\left(\frac{r}{\lambda}\right)\sin\left(\frac{r}{\lambda}\right) -\left(\frac{r}{\lambda}\right)^2\cos\left(\frac{r}{\lambda}\right)\right] \equiv C_{3,\mathrm{ret}}^{^{2S+1}\Pi_g}(r), \tag{9}$$

where $\lambda = \lambda_{SP}/2\pi$ is the wavelength of light associated with the atomic ^2S–^2P transition, which for ^{6}Li is implicitly given in the caption to Table VII.

The only C_m terms used in the analysis of [38] were $C_3^{^3\Sigma_g^+}$, $C_3^{^1\Pi_g}$, $C_3^{^3\Pi_g}$, $C_6^{^3\Sigma_g^+}$, and $C_8^{^3\Sigma_g^+}$ since the $C_{6/8}^{^{2S+1}\Pi_g}$ terms were found not to have a significant effect on the $1^3\Sigma_g^+$ potential. Though fairly accurate values for all three C_{10} terms involved were available (with the infinite mass approximation) as early as 2007 [43], their effects were not considered in [38] due to the unavailability of the values for the three C_9 terms (which emerge in third-order perturbation theory) involved. Now that values for the involved C_9 and C_{11} terms have been reported (with the infinite mass approximation) in [44], we are able to consider all terms appearing in Eq. (7) up to and including the C_{11} terms. However, Fig. 6 shows that none of these C_9, C_{10}, or C_{11} terms seem to have a noticeable effect on the potential in our data region, and since including superfluous C_m terms might lead to unphysical behavior in the short- to mid-range regions that lack data [45], we chose to include neither these terms nor the $C_{6/8}^{^{2S+1}\Pi_g}$ terms in our potentials. The C_m values used throughout this paper (including in Fig. 6) are presented in Table VI, along with details about how each of them was calculated, and their sources. The calculations that were done with the Hylleraas-type basis set are the most accurate; however, no such calculation has been published for the C_{10} values, so for Fig. 6 we used the values from [43], which were calculated using the Laguerre-type orbital (LTO) basis. The only values for $C_{9,10,11}$ that have been published were calculated with the approximation that the mass of Li is infinite, while finite mass corrections have been included to calculate $C_{3,6,8}$ for ^{6}Li in [46]. While we use these ^{6}Li values for $C_{6,8}$, we use the ^{7}Li values for C_3 published in [47], which are likely [48] to be closer to the

TABLE VI. C_m coefficients used in our refined potential. Numbers in parentheses are the uncertainties in the last digits shown.

	$\mathrm{Li}_2(1^3\Sigma_g^+)$	$\mathrm{Li}_2(1^1\Pi_g)$	$\mathrm{Li}_2(1^3\Pi_g)$	Basis set	Effective mass	Relativistic corrections	Source
C_3 (cm^{-1}Å^3)	3.57773×10^5	-1.78887×10^5	1.78887×10^5	Hylleraas-type	^{7}Li	✓	[47]
C_6 (cm^{-1}Å^6)	$1.00059(3) \times 10^7$	$6.78183(2) \times 10^6$	$6.78183(2) \times 10^6$	Hylleraas-type	^{6}Li	✘	[46]
C_8 (cm^{-1}Å^8)	$3.69965(8) \times 10^8$	$1.39076(1) \times 10^8$	$6.55441(5) \times 10^8$	Hylleraas-type	^{6}Li	✘	[46]
C_9 (cm^{-1}Å^9)	$1.6340(1) \times 10^8$	$3.694(1) \times 10^7$	$3.694(1) \times 10^7$	Hylleraas-type	$^\infty$Li	✘	[44]
C_{10} (cm^{-1}Å^{10})	1.1374×10^{10}	3.3746×10^9	3.4707×10^8	Laguerre-type	$^\infty$Li	✘	[43]
C_{11} (cm^{-1}Å^{11})	-1.186×10^{10}	1.985×10^{10}	5.304×10^9	Hylleraas-type	$^\infty$Li	✘	[44]

true ^{6}Li values than the ^{6}Li values from [46] since relativistic corrections have been included in the former. The $C_{6,8,10}$ used for the $a^3\Sigma_u^+$ state were nonrelativistic ^{6}Li values from [46] that were calculated with the Hylleraas-type basis set and with finite mass corrections—they are presented in Table VII and are slightly different from the ^{7}Li values used in [38].

The caption to Fig. 6 and the remainder of this paper use the following definitions for notational simplicity:

$$C_m^{\Sigma} \equiv C_m^{^3\Sigma_g^+}, \tag{10}$$

$$C_3^{\Pi} \equiv C_3^{^1\Pi_g} = -C_3^{^3\Pi_g} = \frac{1}{2}C_3^{\Sigma}. \tag{11}$$

Equation (11) also presents useful symmetry relations (see Ref. [10] and references therein).

Finally, as described in [28,38], the long-range part of the potential can be modeled more accurately with the inclusion of another set of adjustments. Following [28,38], we define $C_6^{\Sigma,\text{adj}} \equiv C_6^{\Sigma} + (C_{3,\text{ret}}^{\Sigma})^2/(4\mathfrak{D}_e)$ and $C_9^{\text{adj}} \equiv C_{3,\text{ret}}^{\Sigma}C_6^{\Sigma,\text{adj}}/(2\mathfrak{D}_e)$. Using these adjustments, along with the treatment of the retardation effect and the removal of the negligible C_m terms mentioned in the caption of Fig. 6, brings us to the definition of $u_{\text{LR}}(r)$ we use for this study (which happens to have the same form as that in [38], though the C_m values used are those in Table VI rather than those used in [38]),

$$u_{\text{LR}}(r) = -\lambda_{\text{min}}^{\text{adj}}\left(C_{3,\text{ret}}^{\Sigma}, C_{3,\text{ret}}^{\Pi}, C_6^{\Sigma,\text{adj}}, C_8^{\Sigma}; r\right) + C_9^{\Sigma,\text{adj}}/r^9, \tag{12}$$

where $\lambda_{\text{min}}^{\text{adj}}(r)$ is defined as the lowest eigenenergy of the following matrix $\mathbf{M}_{\text{LR}}^{\text{adj}}$ which is a modified version of Eq. (7),

$$\mathbf{M}_{\text{LR}}^{\text{adj}} = \begin{pmatrix} -\frac{1}{3}\left(\frac{C_{3,\text{ret}}^{\Sigma}}{r^3} + \frac{C_6^{\Sigma,\text{adj}}}{r^6} + \frac{C_8^{\Sigma}}{r^8}\right) & \frac{\sqrt{2}}{3}\left(\frac{C_{3,\text{ret}}^{\Sigma}}{r^3} + \frac{C_6^{\Sigma,\text{adj}}}{r^6} + \frac{C_8^{\Sigma}}{r^8}\right) & \frac{2}{\sqrt{6}}\left(\frac{C_{3,\text{ret}}^{\Pi}}{r^3}\right) \\ \frac{\sqrt{2}}{3}\left(\frac{C_{3,\text{ret}}^{\Sigma}}{r^3} + \frac{C_6^{\Sigma,\text{adj}}}{r^6} + \frac{C_8^{\Sigma}}{r^8}\right) & \Delta E - \frac{2}{3}\left(\frac{C_{3,\text{ret}}^{\Sigma}}{r^3} + \frac{C_6^{\Sigma,\text{adj}}}{r^6} + \frac{C_8^{\Sigma}}{r^8}\right) & \frac{1}{\sqrt{3}}\left(\frac{C_{3,\text{ret}}^{\Pi}}{r^3}\right) \\ \frac{2}{\sqrt{6}}\left(\frac{C_{3,\text{ret}}^{\Pi}}{r^3}\right) & \frac{1}{\sqrt{3}}\left(\frac{C_{3,\text{ret}}^{\Pi}}{r^3}\right) & \Delta E \end{pmatrix}. \tag{13}$$

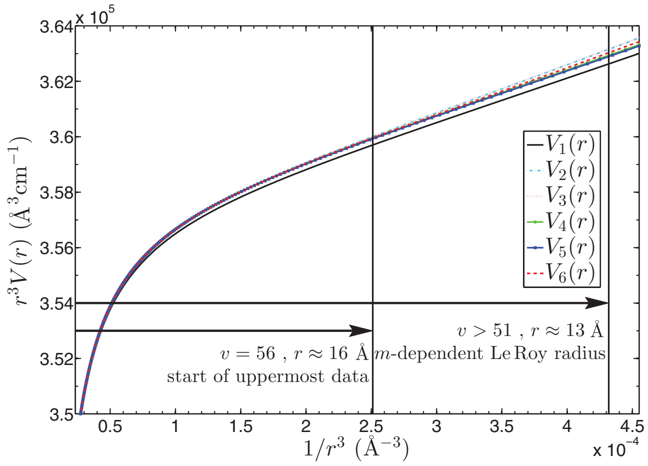

FIG. 6. (Color online) Long range potentials in Le Roy space demonstrating that all C_9, C_{10}, and C_{11} terms appearing in Eq. (7) do not contribute significantly to λ_{min} for the four vibrational levels between the m-dependent Le Roy radius (taken from [44]) and the long-range data region, and especially do not contribute much in the long-range data region. $V_1(r)$ is the experimentally determined potential-energy curve from Ref. [38]. $V_6(r)$ is the theoretical nonretarded long-range potential of Aubert-Frécon [10] in which all C_m coefficients are included from $C_3^{\Sigma,\Pi}$ to $C_{11}^{\Sigma,{}^1\Pi_g,{}^3\Pi_g}$, at the values given in Table VI. $V_2(r)$ is the same as $V_6(r)$ but with $C_{6,8,9,10,11}^{^1\Pi_g,{}^3\Pi_g} = 0$. This shows that these $C_m^{^1\Pi_g,{}^3\Pi_g}$ coefficients are unnecessary. $V_3(r)$ is the same as $V_2(r)$ but also with $C_{11}^{\Sigma} = 0$ and shows that C_{11}^{Σ} is unnecessary. $V_4(r)$ is the same as $V_3(r)$ but also with $C_{10}^{\Sigma} = 0$, which shows that C_{10}^{Σ} is unnecessary. $V_5(r)$ is the same as $V_4(r)$ but also with $C_9^{\Sigma} = 0$, which shows that C_9^{Σ} is unnecessary.

To treat more than one isotopologue of Li$_2$($1^3\Sigma_g^+$), we include Born-Oppenheimer breakdown (BOB) corrections in the same way as described in Sec. 2.4 and Eqs. (3)–(7) of [38]. Since this study is focused on the ^{6,6}Li$_2$ isotopologue, we chose to make this the "reference isotopologue" (as defined after Eq. (3) in [38]), rather than ^{7,7}Li$_2$, which was the reference isotopologue in [38].

As in [38], since most of the rovibrational observations of the $1^3\Sigma_g^+$ state of Li$_2$ were FTIR emissions from the $1^3\Sigma_g^+$ state into the $a^3\Sigma_u^+$ state [7,8], our DPF is a multistate fit to MLR potential models for each of these states. The term values of the relatively small number of observed rovibrational energies from perturbation-facilitated optical-optical double resonance (PFOODR) emissions from the $2^3\Pi_g$ state into the $a^3\Sigma_u^+$ state of ^{7,7}Li$_2$ [49] were treated as fitting parameters in the fit.

Since no new data for Li$_2$($a^3\Sigma_u^+$) is being considered, we chose to use the MLR$_{5,3}^{8,0}$(3)-d model for this state, just as in the final potential reported in Table II of [38], except with the parameters reoptimized by the multistate fit to the current data set. This is the data set described in Table I of [38], but expanded to include the $J = N = 1$ column (the first column) of Table I of the present paper. The "d" in the name for the MLR model is used to indicate that damping functions are included in the model to take into account the weakening of interactions due to the overlap of the electronic wave functions of the interacting atoms, as described in [29]. The Li$_2$($a^3\Sigma_u^+$) potentials used for the present work use damping functions that are defined exactly as in Eqs. (12) and (13) of [38]; and as in [38], the present paper neglects damping functions for the $1^3\Sigma_g^+$ state for simplicity.

The MLR model chosen in [38] for the final Li$_2$($1^3\Sigma_g^+$) potential presented in Table II of that paper was of the form MLR$_{6,3}^{3,8}$(9). When the parameters of an MLR$_{6,3}^{3,8}$(9) model are reoptimized by a fit to the current data set, the resulting

TABLE VII. Parameters defining our recommended MLR potentials. Parameters in square brackets were held fixed in the fit, while numbers in parentheses are 95% confidence limit uncertainties in the last digit(s) shown. The analysis used the ^{6}Li $^2P_{1/2} \leftarrow {}^2S_{1/2}$ excitation energy of $1/\lambda_{SP} \equiv D1 = 14903.2967364$ cm^{-1} from [52], and the ^{6}Li $^2P_{3/2} \leftarrow {}^2P_{1/2}$ spin-orbit splitting energy of $\Delta E \equiv D2 - D1 = 0.3353246$ cm^{-1} with $D2$ from [53]. Units of length and energy are Å and cm^{-1} respectively, and the polynomial coefficients β_i are dimensionless. $\overline{dd} = 0.791$.

	$a(1\,^3\Sigma_u^+)$		$c(1\,^3\Sigma_g^+)$
$\mathfrak{D}_e$	333.7795(62)		7093.4926(86)
r_e	4.170006(32)		3.065436(16)
C_6	[6.7190×10^6]	C_3^Σ	$3.576828(44) \times 10^5$
C_8	[1.12635×10^8]	C_6^Σ	[1.00059×10^7]
C_{10}	[2.78694×10^9]	C_8^Σ	[3.69965×10^8]
ρ_{Li}	[0.54]		[∞]
$\{p,q\}$	{5,3}		{6,2}
r_{ref}	[8.0]		[4.8]
β_0	− 0.516129		− 1.819413208
β_1	− 0.0980		− 0.4729259
β_2	0.1133		− 0.518639
β_3	− 0.0251		− 0.16109
β_4			− 0.8608
β_5			3.933
β_6			0.965
β_7			− 2.81
β_8			− 2.27
β_9			1.2
$\{p_{\mathrm{ad}},q_{\mathrm{ad}}\}$	{6,6}		{3,3}
u_0	0.069(12)		1.596(8)
u_1			3.1(4)
u_2			− 1.5
u_3			− 2.0
u_∞	[0.0]		[1.2315155]

potential predicts the rovibrational energies very well within their respective experimental uncertainty ranges (on average, over the entire data set). However, with the additional data (that happens to lie in a region of the potential about which studies previous to this one had no experimental information), it quickly became apparent that slightly different MLR models could give better fits to the experimental data, and are more robust for predicting the physical parameters C_3, R_e, and D_e. For MLR models different from $\mathrm{MLR}_{6,3}^{3.8}(9)$, we obtained starting parameters for the least-squares fitting from the freely available program `betaFIT` [50]. Parameters from `betaFIT` were first reoptimized using `DPotFit` to the current data set, but with an upper limit set for v. The resulting parameters were then reoptimized again with `DPotFit` to the full current data set.

We focused our studies on $\mathrm{MLR}_{p,q}^{r_{\mathrm{ref}}}(N_\beta)$ models with $p = 6$ since p must be larger than 5, and making it 7 or larger may require a much larger N_β [45]. Of all the $(p,q) = (6,1\text{–}4)$ potentials calculated, the $\mathrm{MLR}_{6,2}^{4.8}(9)$ model stood out as having the best balance of reproducing the experimental data closely, maintaining a low value of N_β, and predicting C_3, R_e, and D_e values that are consistent with a large number of other MLR models. The $\mathrm{MLR}_{6,2}^{r_{\mathrm{ref}}}(8)$ models were also excellent for $4.5 \leqslant r_{\mathrm{ref}} \leqslant 4.8$, but the predictions of C_3, R_e, and D_e were not as consistent with respect to r_{ref} as they were with higher N_β values. While in [38] $q < 3$ was not considered due to the fact that models with low q values have more of a tendency to result in potentials with inflection points on the inner wall, the added data considered in this study significantly reduced the tendency for inflection points to appear on the inner wall of the $q = 3$ potentials, and inflections did not appear here for $q = 2$ in the regime surrounding $(N_\beta, r_{\mathrm{ref}}) = (9,4.8)$. For models with $q = 1$, it was challenging to find the global minima in the least-squares fitting procedure; and for modest values of N_β, potentials in our test cases that reproduced the experimental energies more closely with $q = 1$ than with $q \in \{2,3\}$ were not found. Finally, with the $1^3\Sigma_g^+$ state modeled by an $\mathrm{MLR}_{6,2}^{4.8}(9)$ function, and the $a^3\Sigma_u^+$ modeled by an $\mathrm{MLR}_{5,3}^{8.0}(3)$-d function, it was found that the appropriate number of BOB terms did not change from [38] (adding two adiabatic or nonadiabatic BOB terms still did not significantly improve the fit to the data for the $1^3\Sigma_g^+$ state, and reducing the number of adiabatic BOB terms by just one for the $1^3\Sigma_g^+$ state had a noteworthy effect on the quality of the fit to the data).

This analysis for choosing the model was done without the sequential rounding and re-fitting (SRR) procedure of [51]. Once the $\mathrm{MLR}_{6,2}^{r_{\mathrm{ref}}}(9)$ model was chosen, and the appropriate number of BOB terms was chosen, the SRR procedure was applied. First `DPotFit` was run with all fitting parameters free. Then C_3 for the $1^3\Sigma_g^+$ state was manually rounded to the second digit of its 95% confidence limit uncertainty and `DPotFit` was rerun with this rounded C_3 value fixed and with the rest of the fitting parameters free. Then the r_e values for both states were manually rounded in the same way as C_3 was, and `DPotFit` was rerun with these rounded r_e values fixed and with the remaining fitting parameters free. Finally, $\mathfrak{D}_e$ for both states were rounded manually in the same way as C_3 was, and `DPotFit` was run with these $\mathfrak{D}_e$ values fixed, with all the remaining fitting parameters free, and with `IROUND` $= -1$.

The final potentials for the $a^3\Sigma_u^+$ and $1^3\Sigma_g^+$ states after this SRR procedure are given in Table VII. The dimensionless root-mean-square deviation (labeled $\overline{dd}$, and defined by Eq. (2) of [38]) of this overall multistate fit after the SRR procedure was 0.791, which is less than 0.3% higher than in [38] where $\overline{dd}$ was 0.789, despite the very high accuracy of the additional observed levels, making the fit much more demanding. The fact that $\overline{dd} < 1$ means that the rovibrational energies predicted by the fitted potentials match the observed values to well within their experimental uncertainties (on average, over the entire data set). In Table VIII, the $J = N = 1$ energies for the seven vibrational levels experimentally found in this work are compared to the energies predicted by the refined potential in Table VII, and to those of the potential from Table IIb of the Supplemental Material of [38], which were calculated without knowledge of these seven additional energies.

Potentials for the $^{7,7}\mathrm{Li}_2$ isotopologue can be obtained from those for $^{6,6}\mathrm{Li}_2$ that were presented in Table VII, by using the BOB corrections as described in Sec. 2.4 and Eqs. (3)–(7) of [38].

There is currently a discrepancy between the $1^3\Sigma_g^+$ state C_3 value obtained from experiments [28,38] and from *ab initio*

TABLE VIII. Comparison of the $J = N = 1$ binding energies, found experimentally in this work, to the energies predicted by the refined potential in Table VII and the potential in Table IIb in the Supplemental Material of [38]. All energies are in cm^{-1}, and the predicted energies are represented as the predicted (calculated) energy minus the experimental (observed) energy. In our measurements, the initial free atomic state is $2a_{2s}$ below the hyperfine center of gravity of the $2S_{1/2} + 2S_{1/2}$ threshold (where a_{2s} for ^{6}Li is 152.137 MHz [58]). Consequently, the binding energy is computed by adding 304.274 MHz to the $D1$ transition frequency and subtracting our measured frequency for the PA loss feature.

v'	This work (experimental)	This work (predicted) Calc. − obs.	Ref. [38] (predicted) Calc. − obs.
20	$2666.12934 \pm 2 \times 10^{-5}$	-2.60×10^{-6}	-0.525
21	$2508.90963 \pm 2 \times 10^{-5}$	1.41×10^{-5}	-0.648
22	$2357.23922 \pm 2 \times 10^{-5}$	-9.80×10^{-7}	-0.781
23	$2211.13373 \pm 2 \times 10^{-5}$	-1.07×10^{-5}	-0.920
24	$2070.60609 \pm 2 \times 10^{-5}$	-1.77×10^{-6}	-1.059
25	$1935.66542 \pm 2 \times 10^{-5}$	1.51×10^{-5}	-1.194
26	$1806.31575 \pm 2 \times 10^{-5}$	-8.91×10^{-6}	-1.319

calculations [47] (see also [44]). The most accurate estimate of the ^{6}Li C_3 value for this state is 3.57773×10^5 cm^{-1}Å^3 from [47], which was actually calculated for ^{7}Li but is expected to be more accurate than any other currently known estimate for ^{6}Li [48] since it was calculated with relativistic effects included. The value of C_3 that came from the fit in 2009 [28] of an MLR model potential for the $A(1^1\Sigma_u^+)$ state to experimental data was larger than this *ab initio* value, and the value from the fit in 2011 [38] to an MLR potential model for the $c(1^3\Sigma_g^+)$ state was smaller than the *ab initio* value. The additional data used in this analysis brought the fitted value of $C_3 = (3.576828 \pm 0.000044) \times 10^5$ cm^{-1}Å^3 from this study closer to the *ab initio* value than that from [38], but it is still significantly smaller than the *ab initio* value, meaning that more data for the $1^3\Sigma_g^+$ state is perhaps required to resolve the current discrepancy between experiment and theory.

VI. CONCLUSIONS

In summary, we have measured the binding energies of seven vibrational levels $v' = 20$–26 of the $1^3\Sigma_g^+$ excited state of ^{6}Li$_2$ molecules with an absolute uncertainty of ± 0.00002 cm^{-1} (± 600 kHz) by photoassociating a quantum degenerate Fermi gas of lithium atoms. For each vibrational state, we provide measurements of the three rotational states $N' = 0,1,2$. In addition, we observe a splitting of the $N' = 1$ excited state due to spin-spin and spin-rotation interactions and we use our data to extract the corresponding interaction constants. We also use our data to further refine the analytic potential-energy function for this state and provide the updated Morse/long-range model parameters. These measurements and refined potential provide a starting point to map the 10 bound levels of the ground triplet state $a^3\Sigma_u^+$ of ^{6,6}Li$_2$ and the 11 bound levels of the $a^3\Sigma_u^+$ state of ^{7,7}Li$_2$ by two-color photoassociation [54], and to eventually transfer Feshbach molecules into one of these ground-state levels using a two-photon stimulated Raman adiabatic passage (STIRAP) process [55]. Molecules in the triplet rovibrational ground state can, in theory, relax to the singlet state $X^1\Sigma_g^+$ via inelastic collisions; however, this process, which requires a change of the spin configuration, may be suppressed by weak couplings in the ground state resulting in a spin-blockade metastability of the triplet state. Such a metastability would be very interesting for the study of ultracold controlled chemistry, as ground-state triplet molecules possess a magnetic moment and collisions between them should exhibit magnetically tunable scattering resonances [56]. In addition, work has been done that shows that ground-state homonuclear molecules with rotational quantum number $N = 1$ may be collisionally stable, and these exhibit long-range anisotropic quadrupole-quadrupole interactions [57]. Finally, metastable triplet state molecules might be a good candidate for experiments on the alignment and spinning of ultracold molecules with high-intensity, ultrashort pulsed lasers.

ACKNOWLEDGMENTS

We gratefully acknowledge Takamasa Momose for the use of the Ti:sapphire laser. We also thank Robert J Le Roy for many helpful discussions, and Jim Mitroy for advice on which C_m values to use. The authors also acknowledge financial support from the Canadian Institute for Advanced Research (CIfAR), the Natural Sciences and Engineering Research Council of Canada (NSERC/CRSNG), and the Canadian Foundation for Innovation (CFI). N.S.D. also thanks the Clarendon Fund for financial support.

---

[1] J. Weiner, V. S. Bagnato, S. Zilio, and P. S. Julienne, Rev. Mod. Phys. **71**, 1 (1999).

[2] W. Stwalley and H. Wang, J. Mol. Spectrosc. **195**, 194 (1999).

[3] J. Bahns, W. Stwalley, and P. Gould, Adv. At. Mol. Opt. Phys. **42**, 171 (2000).

[4] F. Masnou-Seeuws and P. Pillet, Adv. At. Mol. Opt. Phys. **47**, 53 (2001).

[5] K. M. Jones, E. Tiesinga, P. D. Lett, and P. S. Julienne, Rev. Mod. Phys. **78**, 483 (2006).

[6] E. R. I. Abraham, W. I. McAlexander, H. T. C. Stoof, and R. G. Hulet, Phys. Rev. A **53**, 3092 (1996).

[7] F. Martin, R. Bacis, J. Vergs, C. Linton, G. Bujin, C. Cheng, and E. Stad, Spectrochim. Acta, Part A **44**, 1369 (1988).

[8] C. Linton, T. L. Murphy, F. Martin, R. Bacis, and J. Verges, J. Chem. Phys. **91**, 6036 (1989).

[9] E. R. I. Abraham, N. W. M. Ritchie, W. I. McAlexander, and R. G. Hulet, J. Chem. Phys. **103**, 7773 (1995).

[10] M. Aubert-Frécon, G. Hadinger, S. Magnier, and S. Rousseau, J. Mol. Spectrosc. **188**, 182 (1998).

[11] J. Deiglmayr, M. Aymar, R. Wester, M. Weidemüller, and O. Dulieu, J. Chem. Phys. **129**, 064309 (2008).

[12] M. Lemeshko and B. Friedrich, Phys. Rev. A **79**, 050501 (2009).

[13] M. Lemeshko and B. Friedrich, Phys. Rev. Lett. **103**, 053003 (2009).

[14] K. Ladouceur, B. G. Klappauf, J. Van Dongen, N. Rauhut, B. Schuster, A. Mills, D. J. Jones, and K. W. Madison, J. Opt. Soc. Am. B **26**, 210 (2009).

[15] B. Deh, W. Gunton, B. G. Klappauf, Z. Li, M. Semczuk, J. Van Dongen, and K. W. Madison, Phys. Rev. A **82**, 020701 (2010).

[16] C. H. Schunck, M. W. Zwierlein, C. A. Stan, S. M. F. Raupach, W. Ketterle, A. Simoni, E. Tiesinga, C. J. Williams, and P. S. Julienne, Phys. Rev. A **71**, 045601 (2005).

[17] R. Cote and A. Dalgarno, J. Mol. Spectrosc. **195**, 236 (1999).

[18] D. A. Steck, Rubidium 85 D Line Data, http://steck.us/alkalidata (rev. 2.1.5, 19 September 2012) (unpublished).

[19] A. K. Mills, Y.-F. Chen, K. W. Madison, and D. J. Jones, J. Opt. Soc. Am. B **26**, 1276 (2009).

[20] M. Haw, Physics & Astronomy Undergraduate Honours Theses, University of British Columbia, 2012, https://circle.ubc.ca/handle/2429/43353.

[21] We verified that the magnetic field was below 400 mG by measuring the transition frequencies between the magnetic sublevels of the $F = 2$ and $F = 3$ ground hyperfine states of ^{85}Rb prepared in the CDT.

[22] The spin purification was performed at a high magnetic field (typically 700 G), where the optical transitions from the $|1\rangle$ and $|2\rangle$ states to the excited $2p_{3/2}$ manifold are well separated. In addition, the field is sufficiently large to disrupt the hyperfine coupling and these transitions become approximately "closed" such that the excited-state atom returns to the original ground state with a large probability, allowing each atom to scatter many photons during the pulse and subsequently leave the trap.

[23] G. Herzberg, *Molecular Spectra and Molecular Structure, I. Spectra of Diatomic Molecules* (Van Nostrand, New York, 1950).

[24] R. Schlapp, Phys. Rev. **39**, 806 (1932).

[25] B. Minaev, Spectrochimica Acta Part A **62**, 790 (2005).

[26] R. J. Le Roy, Y. Huang, and C. Jary, J. Chem. Phys. **125**, 164310 (2006).

[27] R. J. Le Roy and R. D. E. Henderson, Mol. Phys. **105**, 663 (2007).

[28] R. J. Le Roy, N. S. Dattani, J. A. Coxon, A. J. Ross, P. Crozet, and C. Linton, J. Chem. Phys. **131**, 204309 (2009).

[29] R. J. Le Roy, C. C. Haugen, J. Tao, and H. Li, Mol. Phys. **109**, 435 (2011).

[30] H. Salami, A. J. Ross, P. Crozet, W. Jastrzebski, P. Kowalczyk, and R. J. Le Roy, J. Chem. Phys. **126**, 194313 (2007).

[31] A. Shayesteh, R. D. E. Henderson, R. J. Le Roy, and P. F. Bernath, J. Phys. Chem. A **111**, 12495 (2007).

[32] H. Li and R. J. Le Roy, Phys. Chem. Chem. Phys. **10**, 4128 (2008).

[33] J. A. Coxon and P. G. Hajigeorgiou, J. Chem. Phys. **132**, 094105 (2010).

[34] A. Stein, H. Knöckel, and E. Tiemann, Eur. Phys. J. D **57**, 171 (2010).

[35] H. Li, P.-N. Roy, and R. J. Le Roy, J. Chem. Phys. **133**, 104305 (2010).

[36] L. Piticco, F. Merkt, A. A. Cholewinski, F. R. W. McCourt, and R. J. Le Roy, J. Mol. Spectrosc. **264**, 83 (2010).

[37] M. Ivanova, A. Stein, A. Pashov, A. V. Stolyarov, H. Knöckel, and E. Tiemann, J. Chem. Phys. **135**, 174303 (2011).

[38] N. S. Dattani and R. J. Le Roy, J. Mol. Spectrosc. **268**, 199 (2011).

[39] F. Xie, L. Li, D. Li, V. B. Sovkov, K. V. Minaev, V. S. Ivanov, A. M. Lyyra, and S. Magnier, J. Chem. Phys. **135**, 024303 (2011).

[40] M. Steinke, H. Knöckel, and E. Tiemann, Phys. Rev. A **85**, 042720 (2012).

[41] R. J. Le Roy, J. Seto Seto, and Y. Huang, `DPotFit1.2`: A Computer Program for Fitting Diatomic Molecule Spectra to Potential Energy Functions (University of Waterloo Chemical Physics Research Report CP-664, 2007), http://leroy.uwaterloo.ca/programs/

[42] W. J. Meath, J. Chem. Phys. **48**, 227 (1968).

[43] J.-Y. Zhang, J. Mitroy, and M. W. J. Bromley, Phys. Rev. A **75**, 042509 (2007).

[44] L.-Y. Tang, Z.-C. Yan, T.-Y. Shi, and J. Mitroy, Phys. Rev. A **84**, 052502 (2011).

[45] The parameter p in Eqs. (3) and (4) must be larger than the difference between C_{last} and $C_{\text{first}} = C_3$ (see the Supplemental Material of [38] for a derivation of this rule). The larger the value of p, the more β_i parameters that tend to be required in Eq. (4) for a good fit [28]. When too many β_i parameters are used, the potential can become less "rigid" and may extrapolate poorly where data is not available, which can be problematic in this study as there are large gaps in the available experimental energies.

[46] L.-Y. Tang, Z.-C. Yan, T.-Y. Shi, and J. F. Babb, Phys. Rev. A **79**, 062712 (2009).

[47] L.-Y. Tang, J.-Y. Zhang, Z.-C. Yan, T.-Y. Shi, and J. Mitroy, J. Chem. Phys. **133**, 104306 (2010).

[48] J. Mitroy (private communication with N. Dattani, 2012).

[49] C. Linton, F. Martin, A.J. Ross, I. Russier, P. Crozet, A. Yiannopoulou, L. Li, and A.M. Lyyra, J. Mol. Spec. **196**, 20 (1999).

[50] R. J. Le Roy, `betaFIT` 2.0: A Computer Program to Fit Pointwise Potentials to Selected Analytic Functions (University of Waterloo Chemical Physics Research Report CP-665, 2009), http://leroy.uwaterloo.ca/programs/

[51] R. J. Le Roy, J. Mol. Spec. **191**, 223 (1998).

[52] C. J. Sansonetti, C. E. Simien, J. D. Gillaspy, J. N. Tan, S. M. Brewer, R. C. Brown, S. Wu, and J. V. Porto, Phys. Rev. Lett. **107**, 023001 (2011).

[53] R. C. Brown, S. Wu, J. V. Porto, C. J. Sansonetti, C. E. Simien, S. M. Brewer, J. N. Tan, and J. D. Gillaspy, Phys. Rev. A **87**, 032504 (2013).

[54] U. Schlöder, T. Deuschle, C. Silber, and C. Zimmermann, Phys. Rev. A **68**, 051403 (2003).

[55] K.-K. Ni, S. Ospelkaus, M. H. G. de Miranda, A. Pe'er, B. Neyenhuis, J. J. Zirbel, S. Kotochigova, P. S. Julienne, D. S. Jin, and J. Ye, Science **322**, 231 (2008).

[56] R. V. Krems, Phys. Chem. Chem. Phys. **10**, 4079 (2008).

[57] J. Aldegunde and J. M. Hutson, Phys. Rev. A **79**, 013401 (2009).

[58] E. Arimondo, M. Inguscio, and P. Violino, Rev. Mod. Phys. **49**, 31 (1977).